

diploid deletion of 1 of 4,706 ORFs in the yeast genome. We calculated the fitness values for each media condition as the extent of survival and reproduction (fitness) of the deletion strain relative to the pool of all strains grown and measured collectively. Fitness values ( $f$ ) of 1.0 indicate no difference between a single strain and the pool average for that condition;  $f < 1.0$  indicates that the strain is less fit, and  $f > 1.0$  indicates that the strain is more fit than the pool average. In addition, we added to our analysis 1,060 ORFs that each had a lethal effect when deleted and assayed in YPD; we used only lethal deletions that could be inferred as lethal from both of the two studies conducted<sup>11,19</sup>. We divided all genes into four groups according to the  $f$  value as follows: (1) if  $f > 0.95$  for all five media conditions<sup>11</sup>, the deletion has a weak or no fitness effect in all conditions; (2) if  $0.8 \leq f_{\min} < 0.95$ , where  $f_{\min}$  is the smallest  $f$  value for all five growth conditions, the deletion has a moderate effect; (3) if  $0 < f_{\min} < 0.8$ , the deletion has a strong effect; and (4) if the deletion is lethal, we set  $f = 0$ .

## Identification of duplicate and singleton genes

An all-against-all FASTA<sup>17</sup> search was conducted for the whole set of *S. cerevisiae* protein sequences (downloaded from SGD, <http://genome-www.stanford.edu/Saccharomyces/>). A single-copy gene (that is, a singleton) was defined as a protein that did not hit any other proteins in the FASTA search with  $E = 0.1$ ; this loose similarity search criterion was used to make sure that a singleton is indeed a singleton. (An even looser criterion  $E = 1$  was also used in the definition of singleton genes but the results were essentially the same.) Duplicate genes were identified as described<sup>20</sup> except that the criterion of 80% alignable regions between protein sequences was reduced to 50%, because the 80% requirement can miss some duplicate genes. This relaxed criterion is still conservative for identifying duplicate genes; but because we wanted to detect the differences in fitness effects between real duplicate genes and singletons, we used stringent criteria to define duplicate genes and single genes. For each protein pair that met the homology criteria, the FASTA alignable regions were realigned using ClustalW<sup>21</sup> and the corresponding coding sequences were aligned on the basis of the protein alignments. The number of substitutions per synonymous site ( $K_S$ ) and the number of substitutions per nonsynonymous site ( $K_A$ ) between duplicate genes were estimated by the PAML package<sup>22</sup> using default parameters.

## Estimation of gene expression

The Affymetrix microarray gene expression data were downloaded from a study investigating gene expression in response to environmental changes across the genome<sup>16</sup>. As controls, gene expression was measured at time zero in YPD before each environmental change was conducted. We averaged seven independent time-zero measurements to obtain an estimate of the absolute abundance of each messenger RNA transcript in YPD. Our data showed a very high correlation ( $r = 0.95$ ,  $P = 0$ ) to previous estimates of the absolute abundance of all transcripts in the yeast genome during YPD growth<sup>23</sup>.

Received 29 July; accepted 16 September 2002; doi:10.1038/nature01198.

- Winzler, E. A. *et al.* Functional characterization of the *S. cerevisiae* genome by gene deletion and parallel analysis. *Science* **285**, 901–906 (1999).
- Cadigan, K. M., Grossniklaus, U. & Gehring, W. J. Functional redundancy: the respective roles of the 20 sloppily paired genes in *Drosophila* segmentation. *Proc. Natl Acad. Sci. USA* **91**, 6324–6328 (1994).
- Saga, Y., Yagi, T., Ikawa, Y., Sakakura, T. & Aizawa, S. Mice develop normally without tenascin. *Genes Dev.* **6**, 1821–1831 (1992).
- Gibson, T. J. & Spring, J. Genetic redundancy in vertebrates: polyploidy and persistence of genes encoding multidomain proteins. *Trends Genet.* **14**, 46–49 (1998).
- Normanly, J. & Bartel, B. Redundancy as a way of life—IAA metabolism. *Curr. Opin. Plant Biol.* **2**, 207–213 (1999).
- Brookfield, J. F. Y. Can genes be truly redundant? *Curr. Biol.* **2**, 553–554 (1992).
- Nowak, M. A., Boerlijst, M. C., Cooke, J. & Smith, J. M. Evolution of genetic redundancy. *Nature* **388**, 167–171 (1997).
- Tautz, D. Redundancies, development and the flow of information. *BioEssays* **14**, 263–266 (1992).
- Maslov, S. & Sneppen, K. Specificity and stability in topology of protein networks. *Science* **296**, 910–913 (2002).
- Wagner, A. Robustness against mutations in genetic networks of yeast. *Nature Genet.* **24**, 355–361 (2000).
- Steinmetz, L. M. *et al.* Systematic screen for human disease genes in yeast. *Nature Genet.* **31**, 400–404 (2002).
- Seoighe, C. & Wolfe, K. H. Yeast genome evolution in the post-genome era. *Curr. Opin. Microbiol.* **2**, 548–554 (1999).
- Lynch, M. & Conery, J. S. The evolutionary fate and consequences of duplicate genes. *Science* **290**, 1151–1155 (2000).
- Conant, G. C. & Wagner, A. GenomeHistory: a software tool and its application to fully sequenced genomes. *Nucleic Acids Res.* **30**, 3378–3386 (2002).
- Ohno, S. *Evolution by Gene Duplication* (Springer, Berlin, 1970).
- Causton, H. C. *et al.* Remodeling of yeast genome expression in response to environmental changes. *Mol. Biol. Cell* **12**, 323–337 (2001).
- Pearson, W. R. & Lipman, D. J. Improved tools for biological sequence analysis. *Proc. Natl Acad. Sci. USA* **85**, 2444–2448 (1988).
- Kitami, T. & Nadeau, J. H. Biochemical networking contributes more to genetic buffering in human and mouse metabolic pathways than does gene duplication. *Nature Genet.* **32**, 191–194 (2002).
- Giaever, G. *et al.* Functional profiling of the *Saccharomyces cerevisiae* genome. *Nature* **418**, 387–391 (2002).
- Gu, Z., Cavalcanti, A., Chen, F.-C., Bouman, P. & Li, W.-H. Extent of gene duplication in the genomes of *Drosophila*, nematode, and yeast. *Mol. Biol. Evol.* **19**, 256–262 (2002).
- Thompson, J. D., Higgins, D. G. & Gibson, T. J. CLUSTAL W: improving the sensitivity of progressive multiple sequence alignment through sequence weighting, position-specific gap penalties and weight matrix choice. *Nucleic Acids Res.* **22**, 4673–4680 (1994).

- Yang, Z. & Nielsen, R. Estimating synonymous and nonsynonymous substitution rates under realistic evolutionary models. *Mol. Biol. Evol.* **17**, 32–43 (2000).
- Holstege, F. C. P. *et al.* Dissecting the regulatory circuitry of a eukaryotic genome. *Cell* **95**, 717–728 (1998).

Supplementary Information accompanies the paper on Nature's website (<http://www.nature.com/nature>).

**Acknowledgements** We thank M. Long, T. Oakley, D. Nicolae, K. Thornton, A. Deuschbauer and J. Zhang for discussions and comments. This work was supported by NIH grants to W.H.L. and to R.W.D.

**Competing interests statement** The authors declare that they have no competing financial interests.

**Correspondence** and requests for materials should be addressed to W.H.L. (e-mail: whli@uchicago.edu).

## Synaptic depression in the localization of sound

Daniel L. Cook\*, Peter C. Schwindt\*, Lucinda A. Grande† & William J. Spain\*†‡§

\* Department of Physiology and Biophysics, † Department of Neurology; and § Virginia Merrill Bloedel Hearing Research Center, University of Washington, Seattle, Washington 98105, USA  
 ‡ VA Puget Sound Health Care System, Seattle, Washington 98108, USA

Short-term synaptic plasticity, which is common in the central nervous system, may contribute to the signal processing functions of both temporal integration and coincidence detection<sup>1–3</sup>. For temporal integrators, whose output firing rate depends on a running average of recent synaptic inputs, plasticity modulates input synaptic strength and thus may directly control signalling gain<sup>2</sup> and the function of neural networks<sup>1–4</sup>. But the firing probability of an ideal coincidence detector would depend on the temporal coincidence of events rather than on the average frequency of synaptic events. Here we have examined a specific case of how synaptic plasticity can affect temporal coincidence detection, by experimentally characterizing synaptic depression at the synapse between neurons in the nucleus magnocellularis and coincidence detection neurons in the nucleus laminaris in the chick auditory brainstem<sup>5</sup>. We combine an empirical description of this depression with a biophysical model of signalling in the nucleus laminaris. The resulting model predicts that synaptic depression provides an adaptive mechanism for preserving interaural time-delay information (a proxy for the location of sound in space) despite the confounding effects of sound-intensity-related information. This mechanism may help nucleus laminaris neurons to pass specific sound localization information to higher processing centres.

In the avian auditory brainstem, each neuron of the nucleus laminaris (NL), like the medial superior olive in mammals<sup>6,7</sup>, constitutes an azimuthal 'place code'<sup>8</sup> that is tuned to detect the coincidental arrival of excitatory postsynaptic potentials (EPSPs) generated by ipsi- and contralateral nucleus magnocellularis (NM) neuron action potential firing<sup>9</sup>, which is phase-locked to sound waves arriving at each ear. The intensity of the sound, however, changes the likelihood that an NM cell will fire on a given sound wave cycle, such that increasing sound intensity increases the average NM firing rate and thus the average frequency of NM–NL EPSPs<sup>10</sup>. This increase of NM cell firing rate with sound intensity would be expected to increase the postsynaptic NL cell firing rate,

perhaps even to the saturation limit of its spike-generating mechanism. Because NL cell firing rate encodes sound localization<sup>8</sup>, the saturation of its firing rate will degrade sound localization.

The NL cell firing rate in the owl is remarkably insensitive to sound intensity<sup>11</sup>, however, suggesting that there are mechanisms that minimize the effect of intensity-related inputs to higher centres processing the localization of sound. Three such mechanisms have been postulated: first, the intrinsic membrane properties of chick NL coincidence detectors may limit their firing rate<sup>12</sup>; second, parallel, intensity-related inhibitory afferents to chick and owl NL cells may attenuate the NL responses to high-intensity sound<sup>11,13–15</sup>; and third, nonlinear, saturating summation of EPSPs in NL neuron dendrites may limit excessive input<sup>16</sup>. Here we suggest that the observed synaptic depression at NM–NL synapses may be an additional, independent mechanism for enhancing coincidence detection (and thus sound localization) in the auditory system.

We studied synaptic depression at NM–NL synapses in brainstem slices taken from chicks at embryonic day E18–21 (hearing in chick embryos is established at about E15–17; ref. 17). Figure 1a shows how we used minimally suprathreshold extracellular stimulation of identified NM neurons to elicit EPSPs that were recorded intracellularly from ipsilateral NL neurons. Figure 1b shows an example recording of a 50-Hz stimulus train to an NM neuron in which the EPSP amplitude depressed quickly to a steady-state value much

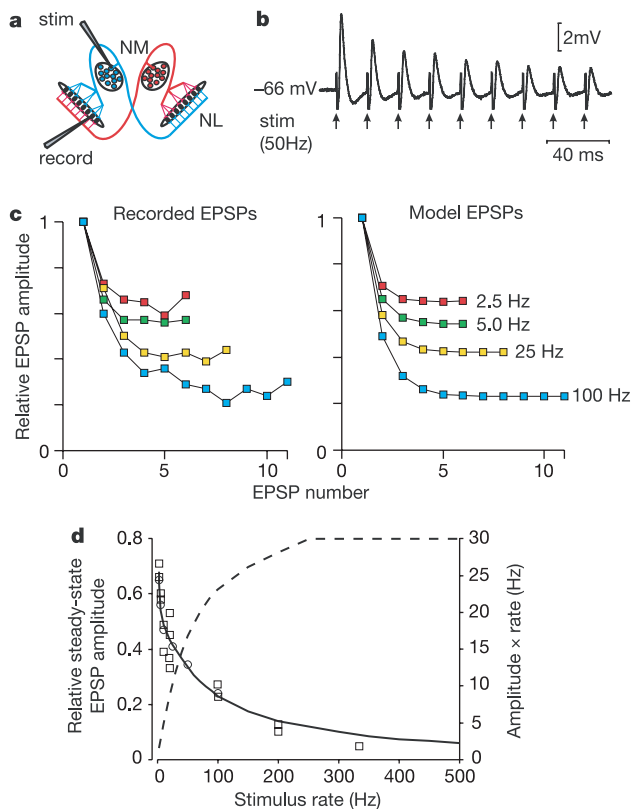


**Figure 1** Synaptic depression at NM–NL synapses. **a**, EPSPs were recorded from NL neuron somata in chick brainstem slices in response to minimal stimulation (stim) of ipsilateral NM cells (duration 0.2–0.6 ms, amplitude 20–50  $\mu$ A). **b**, EPSP amplitudes rapidly decrease on successive stimuli. **c**, Plots of average EPSP amplitude versus EPSP number (15–20 stimulus trains at 2–100 Hz with intertrain intervals of 5–10 s) Left, measured; right, simulated from equation (4). Each EPSP amplitude was normalized to the first EPSP in its train. **d**, Steady-state EPSP amplitude decreases with increasing stimulus rate in a manner closely predicted by the empirical model of synaptic depression (unbroken line). Circles represent data from the cell in **c**; squares represent data from four other cells. The broken line shows that the product of EPSP amplitude times stimulus rate (right axis) reaches a maximum at about 250 Hz and thus defines a ‘limiting frequency’<sup>2,21</sup>.

smaller than the first EPSP. Figure 1c (left) shows the time course of depression at each of four stimulus frequencies for one set of NL cell recordings. Successive EPSPs declined to a steady-state amplitude after five or six EPSPs. The steady-state amplitude was reduced to roughly a third as the stimulus frequency increased from 2 to 100 Hz.

To test the idea that the observed synaptic depression at NM–NL synapses may preserve coincidence detection in NL neurons during increased NM neuron firing, we used NEURON software<sup>18</sup> to model the neuronal circuit shown in Fig. 1a. The model consisted of three key elements: first, synaptic inputs from several ipsi- and contralateral NM neurons converged on a single NL cell; second, an empirically derived model simulated NM–NL synaptic depression (Methods and Fig. 1c, d); and third, a biophysical, compartmental model simulated the unusual EPSP summation and spiking properties of NL cells<sup>12</sup>.

To provide realistic synaptic inputs to NL neurons, we used a stimulus model<sup>10,11,19</sup> that mimics NM neuron firing patterns (Fig. 2). When the sound stimulus is a pure tone (a sinusoidal variation in air pressure), action potentials in a given NM neuron tend to fire at a specific time delay (or phase delay) after the peak of each cycle of the tone stimulus. Such ‘phase-locking’ to the audio signal is not precise, however, because there is a small phase error, called ‘jitter’, in spike timing, which is evident as scatter around the mean in the histograms shown in Fig. 2c. In addition, NM cells fire on only a fraction of sound cycles so that their average firing frequency is always less than the tone frequency (Fig. 2b). But increased sound intensity increases the probability of NM firing, so that the average firing frequency amounts to a proxy variable for sound intensity<sup>10</sup>.

In the computational model, the phase-locked, jittery and prob-

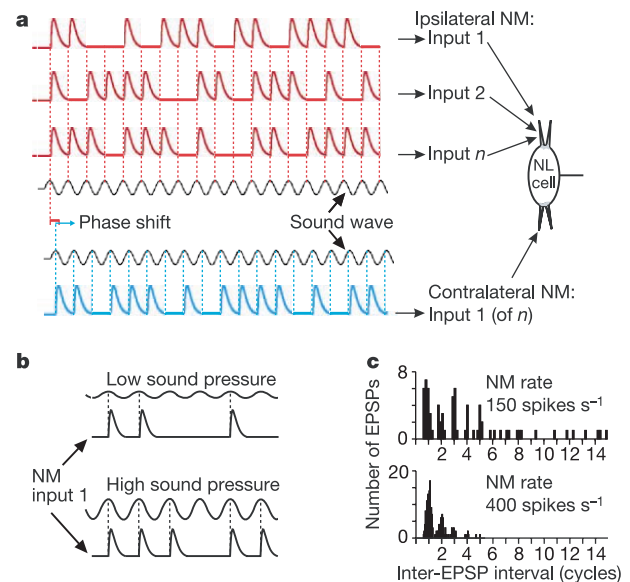


**Figure 2** Simulating phase-locked NM synaptic input to NL neurons. **a**, A pure tone (upper sound waves) arriving at the ipsilateral ear elicits phase-locked NM–NL EPSPs (red traces represent 3 of 72 NM inputs) that converge on one set of dendrites on an NL neuron. The same tone arriving with some phase delay (lower sound wave) at the contralateral ear triggers phase-delayed trains (blue trace represents 1 of 72 inputs) of EPSPs that converge on a second set of dendrites on the NL neuron. The number of EPSPs arriving at the NL cell varies from cycle to cycle, because each NM cell fires once on only a fraction of the sound cycles according to a probability distribution. Included in the model but not shown is the ‘jitter’ of NM firing. **b**, Increasing sound intensity increased the probability per cycle of NM cell firing<sup>10,11</sup>. **c**, An increase in average NM firing rate from 150 to 400  $s^{-1}$  (that is, a change from low to high sound intensity) causes a shortening of the average inter-EPSP interval.

abilistic firing of two sets of 72 independent synapses (one set from ipsi- and one set from contralateral NM cells) converge on opposite sets of NL dendrites. On successive sound cycles, the NL neuron receives a random number of EPSPs because of the probabilistic nature of the NM cell firing. We introduced a phase offset (from 0 to 180°; Fig. 2a) between ipsi- and contralateral NM cell spike trains to represent the interaural time difference (ITD; up to 83 μs for a 600-Hz virtual sound) occasioned by an off-centre sound source. At a phase offset of 0° (corresponding to an on-centre sound source), ipsi- and contralateral inputs from the NM neurons arrive coincidentally on the NL neuron and thus maximize the likelihood of depolarizing the NL neuron to its spike threshold to evoke its maximal firing rate. Increasing the phase delay towards 180° decreases the likelihood of ipsi- and contralateral EPSPs from NM neurons arriving coincidentally, so that the average NL firing rate decreases to a minimum<sup>8,11</sup>.

A synaptic depletion model<sup>20,21</sup> fit well to the observed NM–NL synaptic depression (Fig. 1c, right, and Fig. 1d, unbroken line). Because we did not study the mechanisms underlying NM–NL synaptic depression, we do not claim that depletion accounts for depression at the NM–NL synapse, but use this model simply as a convenient and accurate empirical description of the time course of the observed synaptic depression.

The time course of the postsynaptic conductance increase in the NL dendrites caused by each NM synapse was modelled as an alpha function (see equations (1) and (2) in Methods) with a time constant of 0.26 ms (ref. 12). In runs without synaptic depression, the maximal conductance amplitude ( $G_{\max}$ ) was fixed and independent of NM firing rate. In runs using synaptic depression,  $G_{\max}$  was applied only to the first NM action potential after the onset of a tone, after which synaptic conductance on successive EPSPs was computed by the depletion model (refs 20, 21, and see below).

To simulate the NL cell response to NM–NL EPSPs, we modelled the biophysics of NL cells (Methods) according to our previous findings<sup>12</sup> that, first, unlike classical integrating neurons, NL cells fire only a single initial action potential in response to sustained depolarization (Fig. 3, bottom); and second, NL cells fire reliably during suprathreshold low-frequency input events (Fig. 3, top) but miss events at higher frequencies (Fig. 3, middle).

Our model coincidence detector circuit showed the expected property of a smooth reduction of NL firing rate as phase delay increased from 0 to 180° (Fig. 4a, left). This behaviour was apparent over a range of synaptic conductance values and in the absence of synaptic depression, as long as the average NM cell firing rate (the proxy for sound intensity) was low. But we found that no single value of  $G_{\max}$  could provide coincidence detection at both high and low sound intensities. For example, a  $G_{\max}$  of 1.5 or 2.0 nS worked well at low intensities but offered virtually no discrimination of phase delay (sound location) for the first 90° at high sound intensity (Fig. 4a, right, upper curves). Conversely, a  $G_{\max}$  of 0.5 nS provided coincidence detection at high intensity but no discrimination at low intensity (Fig. 4a, lowest curves).

The above results indicate that  $G_{\max}$  needs to be varied to provide coincidence detection at both low and high NM firing rates (sound intensity). Synaptic depression can provide an automatic mechanism for adjusting  $G_{\max}$  inversely to the NM firing rate to provide roughly the same NL neuron coincidence detection irrespective of sound intensity. This fact is illustrated by Fig. 4b, which shows that the NL phase-delay curves with synaptic depression are tightly clustered for a broad range of sound intensities represented by average NM firing rates from 150 to 450 spikes  $s^{-1}$ . With synaptic depression included in the model, the NL firing rate becomes relatively insensitive to changes in sound intensity, as is observed *in vivo*<sup>11</sup>. Thus, there is a comparable degree of coincidence detection at all sound intensity levels by automatically adjusting the average synaptic conductance inversely to the average input frequency. When the average firing rate of the inputs is greater than the

limiting frequency, the NL neuron behaves like an ideal coincidence detector (that is, sound intensity has almost no effect on firing rate).

Developmental studies have revealed that some synapses show less depression with maturation (for example, see ref. 22). We therefore recalculated the NL firing rate versus phase-delay curves with  $U = 0.2$  and  $G_{\max} = 3.3$  nS (see equation (4) in Methods) to reduce the amount of steady-state depressed synaptic conductance to about 50% of the value that we measured experimentally. The results were similar to those shown in Fig. 4b, in that we obtained non-saturating phase tuning curves over a wide range of sound intensities (data not shown).

The underlying depression of synaptic conductance going from low- to high-intensity sounds is evident in Fig. 4c, where the average synaptic conductance decreased from 1.4 to 0.7 nS as the input average NM firing rate increased from 150 to 400 spikes  $s^{-1}$ . The synaptic conductance decrease during depression, and not some other consequence of the depression kinetics, accounts for the changes in NL cell firing rate, because the coincidence detection curves with depression for 150 and 400 spikes  $s^{-1}$  can be overlaid almost exactly by the curves without synaptic depression in which  $G_{\max}$  was adjusted to 1.4 nS and 0.7 nS (Fig. 4d). These values correspond to the average steady-state conductances attained during depression (Fig. 4c).

Our data show that synaptic depression exists at the NM–NL synapse in auditory signal processing neurons of the avian brainstem. The fast component of the depression kinetics (tens of milliseconds) is significantly faster than those found in most other areas of the brain (hundreds of milliseconds)<sup>2,21</sup>, which perhaps reflects the rapidly firing cells present in the hippocampus<sup>23,24</sup> and the auditory signal processing system<sup>22,25</sup>.

We neither sought nor can we offer a mechanism for the depression that we have described. Instead, we were interested in understanding what role, if any, synaptic depression may have in signal processing according to the model of auditory coincidence detection and sound localization<sup>26</sup>. Towards this goal, we built a computational model to examine whether the measured features of synaptic depression can offer improved sound localization. Our premise is that sound localization by higher centres (beyond NM and NL cells) would benefit from nearly pure coincidence detection by the NL cell, as would be the case if NL cell firing depended primarily on the degree of coincidence of the synaptic events and

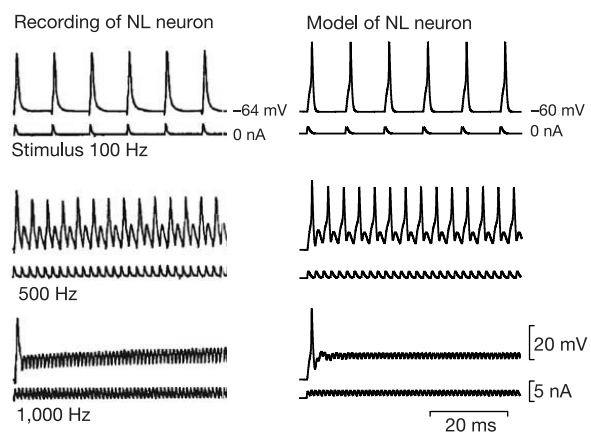


**Figure 3** Distinctive firing properties of chick and model NL neurons. Chick neuron is shown on the left (reproduced, with permission, from ref. 12); model neuron is shown on the right. Top, repetitive suprathreshold stimulation at a low frequency (100 Hz) consistently evokes action potentials. Middle, high-frequency (500 Hz) stimulation fails to trigger action potentials on alternate cycles. Bottom, very high-frequency (1,000 Hz) or direct current (DC) stimulation evokes only a single initial action potential. The ability of these neurons to filter out temporally summated inputs is well suited to their function as coincidence detectors<sup>12</sup>, in contrast to integrating neurons, which fire repetitively to DC inputs.

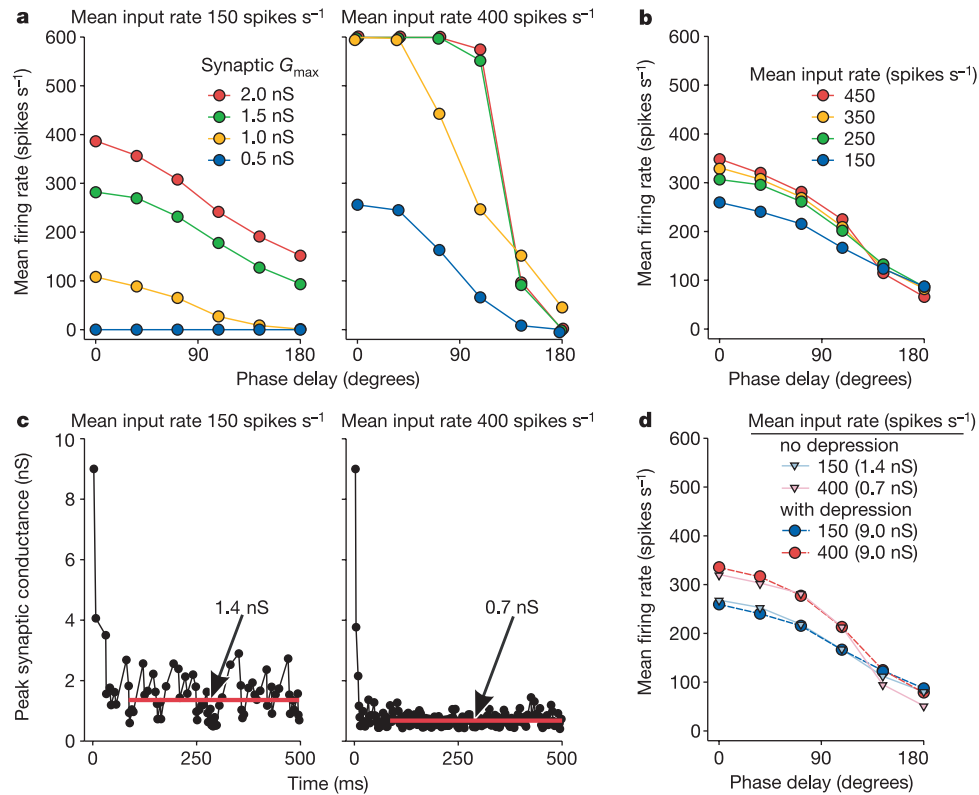


**Figure 4** Synaptic depression buffers coincidence detection against changing sound intensity. **a**, Without synaptic depression, at low sound intensity (average NM input firing rate 150 s<sup>-1</sup>, left) with  $G_{max} < 1.0$  nS, NL output firing depends only weakly on phase delay; but at high sound intensity (400 s<sup>-1</sup>, right) with  $G_{max} > 1.0$  nS, firing rates saturate for phase delays  $< 90^\circ$  and decline to near zero for phase delays near  $180^\circ$ . Curves for low and high intensity are, however, nearly identical for  $G_{max} = 1.5$  and  $G_{max} = 0.5$  nS, respectively. **b**, With synaptic depression, coincidence detection curves converge and, above the limiting frequency (250 s<sup>-1</sup>, Fig. 1d), have little dependence on

input firing rate. Note that synaptic depression also minimizes the reduction in firing rate at long phase delays as sound intensity increases. **c**, Variation of peak event conductance in a single depressing NM-to-NL synapse during a low-intensity (left) and a high-intensity (right) tonal stimulus. Depression reduced average peak synaptic conductance from 1.4 to 0.7 nS as input firing rate increased from 150 to 400 s<sup>-1</sup>. **d**, Preventing event-to-event depression kinetics (apparent in **c**) by fixing  $G_{max}$  at 1.4 and 0.7 nS to correspond to firing rates of 150 and 400 s<sup>-1</sup>, respectively, has no effect on coincidence detection. The sound frequency is 600 Hz in **a-d**.

less so on the frequency of coincidences. Our model shows that synaptic depression can indeed provide an adaptive mechanism that may contribute to the remarkable resistance of NL phase-related spiking (sound localization) to changes of NM cell input spike frequency (sound intensity).

Experimental and theoretical studies have emphasized that synaptic depression allows cortical neurons to function as signal differentiators where the transient response to changes of input firing rate are of paramount importance<sup>2,21</sup>. Here we have emphasized the homeostatic aspect of differentiation, whereby steady-state changes are minimized after the transient response. Thus, the fact that synaptic depression requires the first six (or so) cycles of a tone stimulus to settle to a steady-state (Fig. 4c) correlates well with human psychophysical observations that sound localization improves markedly in the first ~60 ms of a sound stimulus<sup>27</sup> or during the first few milliseconds of binaurally time-shifted sound stimuli that follow a brief masking stimulus in the owl<sup>28</sup>. Any preceding activity of the NM inputs would depress the synaptic conductance to an extent that would prevent saturation of ITD tuning curves at a given intensity. This reasoning suggests that the high spontaneous firing rates observed in NM cells (~90 spikes s<sup>-1</sup>; ref. 10) shorten the time needed for accurate sound localization; in other words, the inputs to NL will always be partially depressed. In the steady-state, if the stimulus frequencies approach or surpass the 'limiting frequency'<sup>2,21</sup> of a synapse (about 250 Hz for the NM-NL synapse according to Fig. 1d), a depressing synapse delivers a nearly constant net synaptic current (that is, the product of frequency and event amplitude and current amplitude) to

the postsynaptic cell. This property of a depressing synapse accounts for the relative insensitivity of the NL cell to input that codes sound intensity (NM cell firing rate) and thus ensures that the degree of input synchronization (coincidence detection) is the variable encoded by the NL cell. For this situation to occur, the kinetics of synaptic depression, which determine the limiting frequency, must be tuned to the range of natural firing frequencies occurring at the synapse. □

## Methods

### Characterization of NM-NL synaptic depression *in vitro*

Chicks at E18–21 were decapitated and a section of the brainstem was removed as described<sup>12</sup>. Brain slices (200  $\mu$ m thick) were cut and perfused in a submerged recording chamber with Ringer's solution that contained (in mM): 130 NaCl, 3 KCl, 2 CaCl<sub>2</sub>, 2 MgCl<sub>2</sub>, 1.2 NaH<sub>2</sub>PO<sub>4</sub>, 26 NaHCO<sub>3</sub> and 10 dextrose, bubbled with 95% O<sub>2</sub> and 5% CO<sub>2</sub> (pH 7.4) at 33–35 °C. The recording chamber was mounted on a fixed stage, upright microscope.

We identified neurons by visualization on a video monitor using infrared-DIC (differential interference contrast) optics. NL neurons were recorded in current clamp using patch pipettes in the whole-cell mode that contained (in mM): 130 KCH<sub>3</sub>SO<sub>4</sub>, 2 MgCl<sub>2</sub>, 5 KCl, 10 HEPES, 2 Na-ATP, 0.2 Na-GTP and 0.1 EGTA (pH 7.2). A monopolar stimulating electrode (a patch pipette filled with Ringer's solution) was placed near the soma of an ipsilateral NM neuron. We varied stimulus intensity to establish the threshold for a mono-amplitude EPSP. The stimulating electrode position was varied to ensure that the EPSP was evoked only by stimulation in a 25- $\mu$ m diameter window. To ensure that the observed EPSP depression reflected changes of synaptic function rather than a systematic change of postsynaptic input conductance, we injected trains of depolarizing currents into the soma. Depression of the current-evoked voltage responses was not seen (data not shown).

### Biophysical model

Our model was implemented in the neurophysiological simulation environment

NEURON<sup>18</sup> using 'hoc' interpreter codes, which are available from W.J.S. on request. Each presynaptic action potential triggered a postsynaptic depolarizing conductance increase that had peak conductance,  $G$ , and a time course described by

$$g(t) = Gxe^{(1-x)} \quad (1)$$

$$\text{where } x = (t - t_{\text{onset}})/\tau_d \quad (2)$$

$\tau_d$  is the time constant governing the conductance increase, and  $t_{\text{onset}}$  is the arrival time of a presynaptic spike. The value of  $\tau_d$  was set to 0.26 ms (ref. 12). If there is no synaptic depression then  $G = G_{\text{max}}$ , otherwise  $G$  varies with the interval since the last transmitter release according to equation (4). The resulting synaptic current,  $I$ , is given by

$$I = g(t) \times (V - E) \quad (3)$$

where  $V$  is membrane potential and  $E$  is current reversal potential (set as 0 mV).

In simulations with synaptic depression, we calculated peak synaptic conductance,  $G_{n+1}$ , for the  $(n + 1)$ th synaptic event during a pure tone sound stimulus using a modified form of equation (2) from ref. 21:

$$G_{n+1} = k[G_n(1 - U)e^{-\Delta t/\tau_f} + G_{\text{max}}(1 - e^{-\Delta t/\tau_f})] + (1 - k)[G_n(1 - U)e^{-\Delta t/\tau_s} + G_{\text{max}}(1 - e^{-\Delta t/\tau_s})] \quad (4)$$

where  $G_{\text{max}}$  (9.0 nS) is the peak synaptic conductance after the synapse has experienced an 'infinite' rest;  $U$  (0.6) is the fraction of available transmitter released;  $\tau_f$  (15 ms) and  $\tau_s$  (1.1 s) are time constants of the fast and slow recovery processes, respectively;  $\Delta t$  is time elapsed since the last transmitter release, and  $k$  (0.3) is the fast fraction of the combined (fast + slow) recovery processes.

The firing pattern for each NM cell is characterized by two independent variables: average firing frequency and the jitter in time of spike initiation. This independence allowed spike frequency and jitter to be computed and varied separately using previously developed algorithms<sup>12</sup>. Spike probability during each sound cycle was given by the ratio of average NM firing rate divided by tone frequency. At cycle onset, a random number between 0 and 1 was drawn from a uniform probability distribution. If this number was less than the spike probability ratio, a spike occurred during that cycle. NM spike jitter was specified as the standard deviation of the dispersion of NM spikes around the phase of the tone where NM cell firing occurred on average. The amount of jitter affects vector strength, an established measure of phase-locking<sup>6</sup>. In these simulations, jitter at each tone frequency was varied as required to produce a vector strength of 0.76, a value measured *in vivo* at a sound frequency of about 600 Hz (ref. 10). Vector strength remains constant for sound intensities >20 dB above threshold<sup>19</sup> and was kept so for all stimulus intensities.

Equations describing the membrane conductances of our NL cell model and its detailed geometry are given in Supplementary Information. Briefly, our model NL cell had a 20- $\mu$ m diameter soma with nine ventral and nine dorsal dendrites<sup>29</sup>, each of which had a uniform distribution of NM synapses around their midpoint. The model behaved like a point neuron because there was minimal attenuation or prolongation of EPSPs transmitted from dendrite to soma. A myelinated axon was connected to the soma by an initial segment to enable unambiguous counting of propagated action potentials. A 'leakage' conductance distributed over the membrane resulted in a hyperpolarizing input conductance of 72 M $\Omega$ , as measured at 37°C (ref. 12). The reversal potential of the leakage current maintained resting potential at -60 mV (ref. 12). The cell contained a Hodgkin-Huxley-like Na<sup>+</sup> and K<sup>+</sup> conductance. The K<sup>+</sup> conductance was based on voltage-clamp measurements made at 37°C in NM neurons<sup>30</sup>, with slight adjustments to match outward rectification in NL cells<sup>12</sup>. The NL cell somatic Na<sup>+</sup> conductance was formulated to replicate several NL spiking properties measured in current clamp<sup>12</sup>.

Received 23 May; accepted 17 October 2002; doi:10.1038/nature01248.

1. Tsodyks, M., Pawelzik, K. & Markram, H. Neural networks with dynamic synapses. *Neural Comput.* **10**, 821–835 (1998).
2. Abbott, L. F., Varela, J. A., Sen, K. & Nelson, S. B. Synaptic depression and cortical gain control. *Science* **275**, 220–224 (1997).
3. Dobrunz, L. E. & Stevens, C. F. Heterogeneity of release probability, facilitation, and depletion at central synapses. *Neuron* **18**, 995–1008 (1997).
4. Nadim, F., Manor, Y., Kopell, N. & Marder, E. Synaptic depression creates a switch that controls the frequency of an oscillatory circuit. *Proc. Natl Acad. Sci. USA* **96**, 8206–8211 (1999).
5. Parks, T. N. & Rubel, E. W. Organization and development of brain stem auditory nuclei of the chicken: organization of projections from n. laminaris. *J. Comp. Neurol.* **164**, 435–448 (1975).
6. Goldberg, J. M. & Brown, P. B. Response of binaural neurons of dog superior olivary complex to dichotic tonal stimuli: some physiological mechanisms of sound localization. *J. Neurophysiol.* **32**, 613–636 (1969).
7. Yin, T. C. & Chan, J. C. Interaural time sensitivity in medial superior olive of cat. *J. Neurophysiol.* **64**, 465–488 (1990).
8. Carr, C. E. & Konishi, M. A circuit for detection of interaural time differences in the brain stem of the barn owl. *J. Neurosci.* **10**, 3227–3246 (1990).
9. Zhou, N. & Parks, T. N. Pharmacology of excitatory amino acid neurotransmission in nucleus laminaris of the chick. *Hear. Res.* **52**, 195–200 (1991).
10. Warchol, M. E. & Dallos, P. Neural coding in the chick cochlear nucleus. *J. Comp. Physiol. A* **166**, 721–734 (1990).
11. Pena, J. L., Viète, S., Albeck, Y. & Konishi, M. Tolerance to sound intensity of binaural coincidence detection in the nucleus laminaris of the owl. *J. Neurosci.* **16**, 7046–7054 (1996).
12. Reyes, A. D., Rubel, E. W. & Spain, W. J. *In vitro* analysis of optimal stimuli for phase-locking and time-delayed modulation of firing in avian nucleus laminaris neurons. *J. Neurosci.* **16**, 993–1007 (1996).
13. Funabiki, K., Koyano, K. & Ohmori, H. The role of GABAergic inputs for coincidence detection in the neurons of nucleus laminaris of the chick. *J. Physiol. (Lond.)* **508**, 851–869 (1998).
14. Bruckner, S. & Hyson, R. L. Effect of GABA on the processing of interaural time differences in nucleus laminaris neurons in the chick. *Eur. J. Neurosci.* **10**, 3438–3450 (1998).

15. Yang, L., Monsivais, P. & Rubel, E. W. The superior olivary nucleus and its influence on nucleus laminaris: a source of inhibitory feedback for coincidence detection in the avian auditory brainstem. *J. Neurosci.* **19**, 2313–2325 (1999).
16. Agmon-Snir, H., Carr, C. E. & Rinzel, J. The role of dendrites in auditory coincidence detection. *Nature* **393**, 268–272 (1998).
17. Jackson, H. & Rubel, E. W. Ontogeny of behavioral responsiveness to sound in the chick embryo as indicated by electrical recordings of motility. *J. Comp. Physiol. Psychol.* **92**, 682–696 (1978).
18. Hines, M. L. & Carnevale, N. T. The NEURON simulation environment. *Neural Comput.* **9**, 1179–1209 (1997).
19. Koppl, C. Phase locking to high frequencies in the auditory nerve and cochlear nucleus magnocellularis of the barn owl, *Tyto alba*. *J. Neurosci.* **17**, 3312–3321 (1997).
20. Lilly, A. W. & North, K. A. K. An electrical investigation of effects of repetitive stimulation on mammalian neuromuscular junction. *J. Neurophysiol.* **16**, 509–527 (1953).
21. Tsodyks, M. V. & Markram, H. The neural code between neocortical pyramidal neurons depends on neurotransmitter release probability. *Proc. Natl Acad. Sci. USA* **94**, 719–723 (1997).
22. Brenowitz, S. & Trussell, L. O. Maturation of synaptic transmission at end-bulb synapses of the cochlear nucleus. *J. Neurosci.* **21**, 9487–9498 (2001).
23. Dobrunz, L. E., Huang, E. P. & Stevens, C. F. Very short-term plasticity in hippocampal synapses. *Proc. Natl Acad. Sci. USA* **94**, 14843–14847 (1997).
24. Harata, N. *et al.* Limited numbers of recycling vesicles in small CNS nerve terminals: implications for neural signaling and vesicular cycling. *Trends Neurosci.* **24**, 637–643 (2001).
25. von Gersdorff, H., Borst, J. & Gerard, G. Short-term plasticity at the calyx of Held. *Nature Rev. Neurosci.* **3**, 55–64 (2002).
26. Jeffress, L. A. Mathematical and electrical models of auditory detection. *J. Acoust. Soc. Am.* **44**, 187–203 (1968).
27. Tobias, J. V. & Zerin, S. Lateralization thresholds as a function of stimulus duration. *J. Acoust. Soc. Am.* **31**, 1591–1594 (1959).
28. Wagner, H. A temporal window for lateralization of interaural time difference by barn owls. *J. Comp. Physiol. A* **169**, 281–289 (1991).
29. Smith, D. J. & Rubel, E. W. Organization and development of brain stem auditory nuclei of the chicken: dendritic gradients in nucleus laminaris. *J. Comp. Neurol.* **186**, 213–239 (1979).
30. Reyes, A. D., Rubel, E. W. & Spain, W. J. Membrane properties underlying the firing of neurons in the avian cochlear nucleus. *J. Neurosci.* **14**, 5352–5364 (1994).

Supplementary Information accompanies the paper on Nature's website (<http://www.nature.com/nature>).

**Acknowledgements** We thank R. Lee for technical help and J. Simon for insight in using NEURON to model sound localization. This work was supported by a VA Merit Review and a grant from the National Institute for Deafness and Communication Disorders.

**Competing interests statement** The authors declare that they have no competing financial interests.

**Correspondence** and requests for materials should be addressed to W.J.S. (e-mail: [spain@u.washington.edu](mailto:spain@u.washington.edu)).

## Extinction-induced upregulation in AMPA receptors reduces cocaine-seeking behaviour

Michael A. Sutton\*†, Eric F. Schmidt\*‡, Kwang-Ho Choi‡, Christina A. Schad\*, Kim Whisler‡, Diana Simmons‡, David A. Karanian\*, Lisa M. Monteggia‡, Rachael L. Neve§ & David W. Self‡

\* Division of Molecular Psychiatry and the Interdepartmental Neuroscience Program, Yale University School of Medicine, New Haven, Connecticut 06520, USA

‡ Department of Psychiatry, The Seay Center for Basic and Applied Research in Psychiatric Illness, The University of Texas Southwestern Medical Center, Dallas, Texas 75390-9070, USA

§ Department of Psychiatry, Harvard Medical School, McLean Hospital, Belmont, Massachusetts 02478, USA

† These authors contributed equally to this work

Cocaine addiction is thought to involve persistent neurobiological changes that facilitate relapse to drug use despite efforts to abstain. But the propensity for relapse may be reduced by extinction training—a form of inhibitory learning that progressively reduces cocaine-seeking behaviour in the absence of cocaine

large inherent dependence on temperature, we concluded that the folding reaction is at least near the Kramers high friction limit.

**Computational**

The double-well potential used was  $g(x) = x^4 - 2x^2$ . Temperature effects were treated as a linear bias along the reaction coordinate,  $t(x, T) = A(T)x$ , where  $A(T)$  is an adjustable parameter for matching the equilibrium data. The folded and unfolded states are separated by 2 distance units along the reaction coordinate, corresponding to a typical helix diffusion length when taken to be nanometres. The population at  $x < 0.83$  was assumed to have the same fluorescence signature as the unfolded state, and at  $x > 0.83$  as the folded state (for compatibility with the three-well model in the Supplementary Information, any value  $x > 0$  yields the same qualitative result). Fluorescence was simulated by convolving populations (for example Fig. 4b) with this response. The one-dimensional Langevin equation with gaussian white noise was integrated by using a fourth-order Runge-Kutta method. A time-step size of 0.01 was used in the integration, and time steps were scaled to match the experimentally observed absolute kinetics. Similar calculations for a three-well model that also matches the data are described in the Supplementary Information.

Received 24 January; accepted 31 March 2003; doi:10.1038/nature01609.

- Berne, B. J. in *Activated Barrier Crossing: Applications in Physics, Chemistry and Biology* (eds Hänggi, P. & Fleming, G. R.) 82–119 (World Scientific, Singapore, 1993).
- Hagen, S. J., Hofrichter, J., Szabo, A. & Eaton, W. A. Diffusion-limited contact formation in unfolded cytochrome c: Estimating the maximum rate of protein folding. *Proc. Natl Acad. Sci. USA* **93**, 11615–11617 (1996).
- Lapidus, L. J., Eaton, W. A. & Hofrichter, J. Measuring the rate of intramolecular contact formation in polypeptides. *Proc. Natl Acad. Sci. USA* **97**, 7220–7225 (2000).
- Bieri, O. *et al.* The speed limit for protein folding measured by triplet-triplet energy transfer. *Proc. Natl Acad. Sci. USA* **96**, 9597–9601 (1999).
- Yeh, I. C. & Hummer, G. Peptide loop-closure kinetics from microsecond molecular dynamics simulations in explicit solvent. *J. Am. Chem. Soc.* **124**, 6563–6568 (2002).
- Thirumalai, D. Time scales for the formation of the most probable tertiary contacts in proteins with applications to cytochrome c. *J. Phys. Chem. B* **103**, 608–610 (1999).
- Portman, J. J., Takada, S. & Wolynes, P. G. Microscopic theory of protein folding rates. II. Local reaction coordinates and chain dynamics. *J. Chem. Phys.* **114**, 5082–5096 (2001).
- Portman, J. J., Takada, S. & Wolynes, P. G. Microscopic theory of protein folding rates. I. Fine structure of the free energy profile and folding routes from a variational approach. *J. Chem. Phys.* **114**, 5069–5081 (2001).
- Hagen, S. J., Hofrichter, J. & Eaton, W. A. Rate of intrachain diffusion of unfolded cytochrome c. *J. Phys. Chem. B* **101**, 2352–2365 (1997).
- Schuler, B., Lipman, E. A. & Eaton, W. A. Probing the free-energy surface for protein folding with single-molecule fluorescence spectroscopy. *Nature* **419**, 743–747 (2002).
- Gruebele, M., Sabelko, J., Ballew, R. & Ervin, J. Laser temperature jump induced protein refolding. *Acc. Chem. Res.* **31**, 699–707 (1998).
- Metzler, R., Klafner, J. & Jortner, J. Hierarchies and logarithmic oscillations in the temporal relaxation patterns of proteins and other complex systems. *Proc. Natl Acad. Sci. USA* **96**, 11085–11089 (1999).
- Burton, R. E., Huang, G. S., Daugherty, M. A., Calderone, T. L. & Oas, T. G. The energy landscape of a fast-folding protein mapped by Ala → Gly substitutions. *Nature Struct. Biol.* **4**, 305–309 (1997).
- Ghaemmaghami, S., Word, J. M., Burton, R. E., Richardson, J. S. & Oas, T. G. Folding kinetics of a fluorescent variant of monomeric lambda repressor. *Biochemistry* **37**, 9179–9185 (1998).
- Myers, J. M. & Oas, T. G. Contribution of a buried hydrogen bond to lambda repressor folding kinetics. *Biochemistry* **38**, 6761–6768 (1999).
- Chang, I. J., Lee, J. C., Winkler, J. R. & Gray, H. B. The protein-folding speed limit: intrachain diffusion times set by electron transfer rates in denatured Ru(NH<sub>3</sub>)<sub>5</sub>(His-33)-Zn-cytochrome c. *Proc. Natl Acad. Sci. USA* **100**, 3838–3840 (2003).
- Silow, M. & Oliveberg, M. Transient aggregates in protein folding are easily mistaken for folding intermediates. *Proc. Natl Acad. Sci. USA* **94**, 6084–6086 (1997).
- Sabelko, J., Ervin, J. & Gruebele, M. Observation of strange kinetics in protein folding. *Proc. Natl Acad. Sci. USA* **96**, 6031–6036 (1999).
- García-Mira, M. M., Sadqi, M., Fischer, N., Sanchez-Ruiz, J. M. & Muñoz, V. Experimental identification of downhill protein folding. *Science* **298**, 2191–2195 (2002).
- Silow, M. & Oliveberg, M. High-energy channeling in protein folding. *Biochemistry* **36**, 7633–7637 (1997).
- Pappenberger, G., Saudan, C., Becker, M., Merbach, A. E. & Kiefhaber, T. Denaturant-induced movement of the transition state of protein folding revealed by high-pressure stopped-flow measurements. *Proc. Natl Acad. Sci. USA* **97**, 17–22 (2002).
- Snow, C. D., Nguyen, H., Pande, V. S. & Gruebele, M. Absolute comparison of simulated and experimental protein-folding dynamics. *Nature* **420**, 102–106 (2002).
- Mayor, U. *et al.* The complete folding pathway of a protein from nanoseconds to microseconds. *Nature* **421**, 863–867 (2003).
- Ervin, J., Sabelko, J. & Gruebele, M. Submicrosecond real-time fluorescence detection: application to protein folding. *J. Photochem. Photobiol. B* **54**, 1–15 (2000).

Supplementary Information accompanies the paper on [www.nature.com/nature](http://www.nature.com/nature).

**Acknowledgements** We thank T. Oas for suggesting many helpful lambda repressor mutations. This work was supported by an Alumni Scholarship and a Camille Dreyfus Teacher-Scholar Award to M.G.

**Competing interests statement** The authors declare that they have no competing financial interests.

**Correspondence** and requests for materials should be addressed to M.G. ([gruebele@scs.uiuc.edu](mailto:gruebele@scs.uiuc.edu)).

erratum

**Antibody neutralization and escape by HIV-1**

Xiping Wei, Julie M. Decker, Shuyi Wang, Huxiong Hui, John C. Kappes, Xiaoyun Wu, Jesus F. Salazar-Gonzalez, Maria G. Salazar, J. Michael Kilby, Michael S. Saag, Natalia L. Komarova, Martin A. Nowak, Beatrice H. Hahn, Peter D. Kwong & George M. Shaw

*Nature* **422**, 307–312 (2003).

In the seventh panel of Fig. 2 of this Letter, the V5 sequence of clone 391-3 appeared incorrectly as: SEKDQTEIFRP. It should read: SKDNQTEIFRP. In addition, there should be no yellow shading (indicating a change in glycosylation) for this sequence. □

corrigenda

**Synaptic depression in the localization of sound**

Daniel L. Cook, Peter C. Schwandt, Lucinda A. Grande & William J. Spain

*Nature* **421**, 66–70 (2003).

It has come to our attention that we failed to cite a relevant study<sup>1</sup> in our Letter. These authors identified the mechanism of synaptic depression measured at the embryonic chick nucleus magno-cellularis to nucleus laminaris synapse as primarily presynaptic, which justifies the synaptic depletion model we used. Furthermore, the narrowing of coincidence detection time windows with EPSP depression as they observed may contribute to the adaptive mechanisms that we described. □

1. Kuba, H., Konomi, K. & Ohmori, H. *Eur. J. Neurosci.* **15**, 984–990 (2002).

**Short interfering RNA confers intracellular antiviral immunity in human cells**

Leonid Gitlin, Sveta Karelsky & Raul Andino

*Nature* **418**, 430–434 (2002).

In Fig. 5a of this Letter, the first and third panels (untreated and siL-treated cells, respectively) should not be identical: the correct figure is shown here. □

